sustainability

Article

Using Ground-Penetrating Radar and Deep Learning to Rapidly Detect Voids and Rebar Defects in Linings

Peng Liu [1], Zude Ding [1,*], Wanping Zhang [1], Zhihua Ren [2] and Xuxiang Yang [2]

[1] Faculty of Civil Engineering and Mechanics, Kunming University of Science and Technology, Kunming 650500, China
[2] Yunnan Institute of Highway Science and Technology, Kunming 650051, China
* Correspondence: dzdvsdt@163.com

Abstract: The geological radar method has found widespread use in evaluating the quality of tunnel lining. However, relying on manual experience to interpret geological radar data may cause identification errors and reduce efficiency when dealing with large numbers of data. This paper proposes a method for identifying internal quality defects in tunnel lining using deep learning and transfer learning techniques. An experimental physical model for detecting the quality of tunnel lining radars was developed to identify the typical radar image features of internal quality defects. Using the geological radar method, a large volume of lining quality detection radar image data was collected, in conjunction with several examples of tunnel engineering. The preprocessing of geological radar data was performed, including gain and normalization, and a set of data samples exhibiting typical lining quality defects was prepared with 6236 detection targets in 4246 images. The intelligent recognition models for tunnel lining quality defects were established using a combination of geological radar image datasets and transfer learning concepts, based on the SSD and YOLOv4 models. The accuracy of the SSD algorithm for cavity defect recognition is 86.58%, with the YOLOv4 algorithm achieving slightly lower accuracy at 86.05%. For steel bar missing recognition, the SSD algorithm has an accuracy of 97.7%, compared to 98.18% accuracy for the YOLOv4 algorithm. This indicates that deep learning-based models are practical for tunnel quality defect detection.

Keywords: lining; ground radar; model experiment; deep learning; transfer learning

check for updates

Citation: Liu, P.; Ding, Z.; Zhang, W.; Ren, Z.; Yang, X. Using Ground-Penetrating Radar and Deep Learning to Rapidly Detect Voids and Rebar Defects in Linings. *Sustainability* **2023**, *15*, 11855. https://doi.org/10.3390/su151511855

Academic Editors: Minh-Tu Cao and Ngoc-Mai Nguyen

Received: 12 June 2023
Revised: 21 July 2023
Accepted: 31 July 2023
Published: 1 August 2023

1. Introduction

In recent years, the continuous expansion of transportation tunnel construction, including highways, railways, and subways, has resulted in a rapid growth in the total mileage of operating tunnels. However, during the tunnel construction procedure, various quality defects such as lining cracks, cavities behind linings, and insufficient lining thickness, as well as leakage, often arise due to different factors, including design, construction, and geological environment. These issues seriously impact the normal use and operational safety of tunnels [1]. Thus, effectively understanding the classification, location, and shape of lining internal defects is crucial in providing the necessary foundations for timely problem solving and ensuring the safety of tunnels [2].

There are common methods used to detect tunnel lining defects, including core drilling and non-destructive testing (NDT) technology [3,4]. Ground-penetrating radar (GPR) is often utilized for its non-destructive, continuous, rapid, and easy-to-operate features, which makes it a popular option in numerous fields such as geological survey, non-destructive testing, roadbed inspection, advanced warning, and underground pipeline. Consequently, it has become the primary option for tunnel lining quality detection [5–7].

Ground-penetrating radar detects targets by identifying differences in the dielectric properties of tunnel lining media. The transmission and receipt of pulsed electromagnetic waves to tunnel linings generate a ground-penetrating radar profile (B-Scan). Internal defects in tunnel linings are detected through analysis of the ground-penetrating radar image [8–10]. However, since the radar data received reflect electromagnetic wave forms only, not the direct imaging of the tunnel lining structure, extensive data processing is required to identify the internal structure of tunnel linings [11,12]. Currently, the interpretation of ground-penetrating radar images relies on manual experience. The efficiency and accuracy of data interpretation largely depend on the professional level of technical personnel. Interpretation efficiency declines significantly when dealing with a large volume of data that prompts time-consuming and laborious manual interpretation processes. As a result, the promotion and use of ground-penetrating radar has been limited.

The conventional recognition algorithms are based on artificial feature extraction followed by classifier classification. Hough transform and SIFT are the commonly used artificial extraction methods [13,14]. The Hough transform algorithm has a high time and space complexity, which makes it inefficient. The SIFT method relies excessively on the gradient direction of local pixel regions, making it susceptible to large errors while processing complex radar images. After feature extraction, a binary classifier such as the support vector machine is frequently employed for classification, but its overall performance has been found to be mediocre [15]. Consequently, the traditional recognition algorithms not only exhibit sub-optimal performance but also encounter difficulties when working with intricate defect images. The enormous volume of tunnel detection issues today has made it even harder for traditional algorithms to cope.

Convolutional neural networks (CNNs) have proven to be robust and versatile in image processing, resulting in widespread use and research across different fields. In image and computer vision, approaches such as FCN [16], U-Net [17], and Segnet [18] have increasingly achieved superior outcomes and are gradually being implemented for autonomous driving systems and other applications. In the medical field, CNNs have also been introduced for defect detection and recognition, resulting in excellent results [19,20]. Similarly, many studies in geophysics have used CNNs and related methods to solve inverse problems [21,22]. In tunnel inspection, Huang et al. [23] utilized the feature hierarchy structure extracted by FCN for the semantic segmentation of subway shield tunnel cracks and leakage defects. They achieved a rapid identification of tunnel defects. Ren et al. [24] effectively solved the segmentation problem of dense pixel-by-pixel tunnel cracks by using an improved deep fully convolutional neural network called CrackSegNet. Yang et al. [25]. employed the finite-difference time-domain (FDTD) method to generate a simulated ground-penetrating radar (GPR) dataset and combined it with a convolutional neural network (SegNet) to achieve the segmentation of internal defects in tunnel linings. Hui et al. [26] created synthetic GPR images using the finite-difference time-domain (FDTD) method and deep convolutional generative adversarial networks (DCGAN). They combined this with deep learning algorithms to achieve the recognition of steel bars, voids, and initial linings in GPR images.

The recognition of defects in ground-penetrating radar (GPR) data images has mainly focused on surface defects in tunnel lining or simulated radar images by past researchers. However, limited research has been carried out on the application of deep learning to interpret measured geological radar images. Therefore, this paper utilizes the popular and efficient single-shot detector (SSD) algorithm and the improved version of the You Only Look Once (YOLOv4) algorithm in object recognition and detection. The theoretical basis of geological radar detection and deep learning is used to process and recognize geological radar data for tunnel lining. By using a measured geological radar dataset and transfer learning methods, the automatic identification of tunnel lining quality defects is achieved. Transfer learning is incorporated to reduce the training data requirement, shorten training time, and improve the network's training effect. The paper covers effective data preparation, CNN selection and analysis, and practical data application. In Section 2, the identification method of tunnel lining defects is introduced, which incorporates the principles of ground-penetrating radar, transfer learning, CNN model principles, and non-maximum suppression. Section 3 describes the collection and processing of real datasets and the conduction of lining model experiments to help establish detection data samples. In Section 4, the prediction effect, accuracy, and overall performance of the tunnel defect recognition model are analyzed. The conclusion summarizes the contributions of this paper.

2. Methodology

This section presents the method proposed in this paper for identifying defects in tunnel lining quality. It encompasses the principles of radar, as well as the widely used and efficient SSD and YOLOv4 algorithms in object recognition and detection. Transfer learning and non-maximum suppression are also included.

2.1. GPR Principle

Ground-penetrating radar (GPR) is a technology that uses ultra-high frequency electromagnetic waves to detect the distribution of internal media structures, and it is commonly utilized in detecting tunnels, highway foundations and pavements, steel structures, cement structures, and more. The working principle of GPR is as follows: the transmitter antenna emits high-frequency electromagnetic waves underground, and the receiving antenna collects the electromagnetic waves reflected back to the ground. As the electromagnetic wave encounters a boundary with different electrical properties in the underground medium, it experiences reflection. The spatial position, structure, morphology, and burial depth of the underground medium can be inferred by analyzing the waveform, amplitude, and variation characteristics of the received electromagnetic waves [27].

In tunnel lining detection, the steel bars, air in cavities, and surrounding concrete exhibit significant electrical property differences, providing a physical basis for GPR usage in detecting lining defects. Figure 1 illustrates the working principle of GPR in detecting lining defects in tunnels.

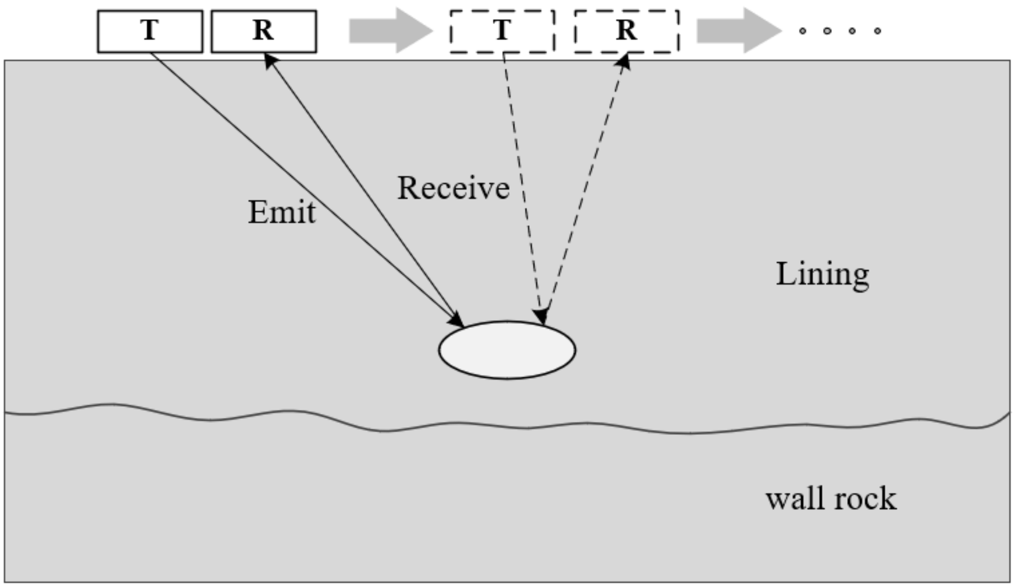

Figure 1. Schematic diagram of the working principle of ground radar.

2.2. Detection Method

This paper presents a method to identify and detect defects in tunnel lining quality. The flowchart for this method is illustrated in Figure 2.

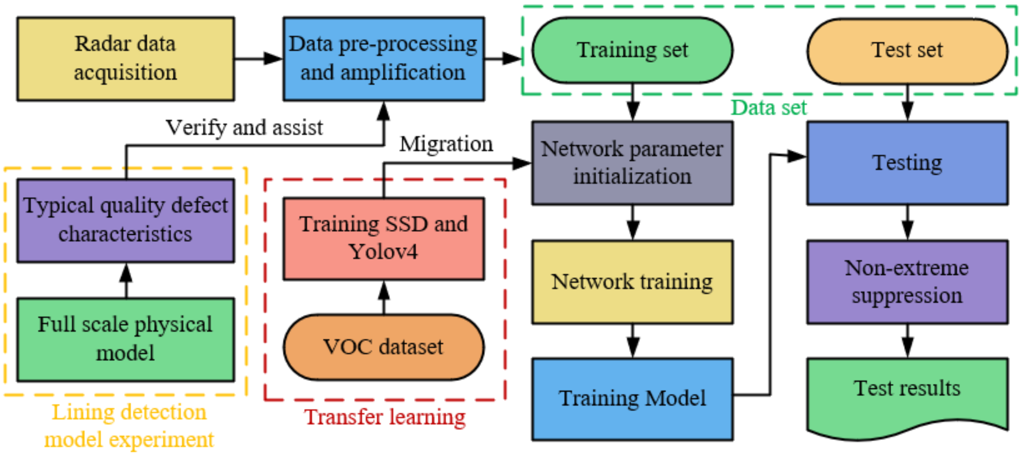

Figure 2. Flowchart of identifying and detecting tunnel lining quality defects.

The radar data are initially collected in the field. Then, a tunnel lining detection model is constructed to assist in the processing of the data, resulting in the formation of the required data set for the detection model. Subsequently, the pre-training of the SSD and YOLOv4 algorithm models is carried out using the VOC image data-set. The initial weight parameters of the detection model in this paper are derived by transferring the parameters of the pre-trained model to the identification of defects in tunnel lining quality through model transfer. The operating code of the detection model is then customized, and the output category number of the model is altered to ensure that the network parameters of the model align with the detection requirements for tunnel lining defects. Finally, the model is trained using processed GPR image data of tunnel lining defects and tested using a test set to detect and identify any defects in tunnel lining quality.

2.3. SSD

The SSD algorithm, which was first introduced at ECCV2016, transforms the object detection task into a regression problem, completing both the localization and classification in a single stage [28]. It has a faster detection speed than Faster R-CNN and a higher detection accuracy than YOLO, thereby achieving an effective balance between the benefits of YOLO and Faster R-CNN. The network structure of the SSD is composed of three parts: the backbone network, the extra layers, and the prediction heads. The backbone network, which is an improved version of VGG16 [29], replaces the last two fully connected layers and the output layer of VGG16 with convolutional layers. The extra layers are four additional convolutional layers that are added to the basic backbone network to generate more features of different scales and improve the ability of the network to recognize the intended features. Additionally, the SSD network uses six convolutional feature maps, namely Conv4_3 (38, 38), Conv7 (19, 19), Conv8_2 (10, 10), Conv9_2 (5, 5), Conv10_2 (3, 3), and Conv11_2 (1, 1). The number of prior boxes used for different scaled feature maps is different (i.e., 30, 60, 111, 162, 213, and 264).

There are three main stages in the SSD algorithm. Firstly, an image is inputted into a pre-trained network to obtain feature maps of varying sizes. After this, features are extracted from the backbone network and the extra layers based on the six mentioned convolutional feature maps, to craft detection branches of varying sizes. These detection branches are then fed into the detection layer for carrying out bounding box regression and classification. Non-maximum suppression (NMS) is used as a final stage to rule out highly overlapping predictions and obtain the optimal solution. Figure 3 depicts the SSD model framework utilized for the recognition of quality defects observed in GPR images.

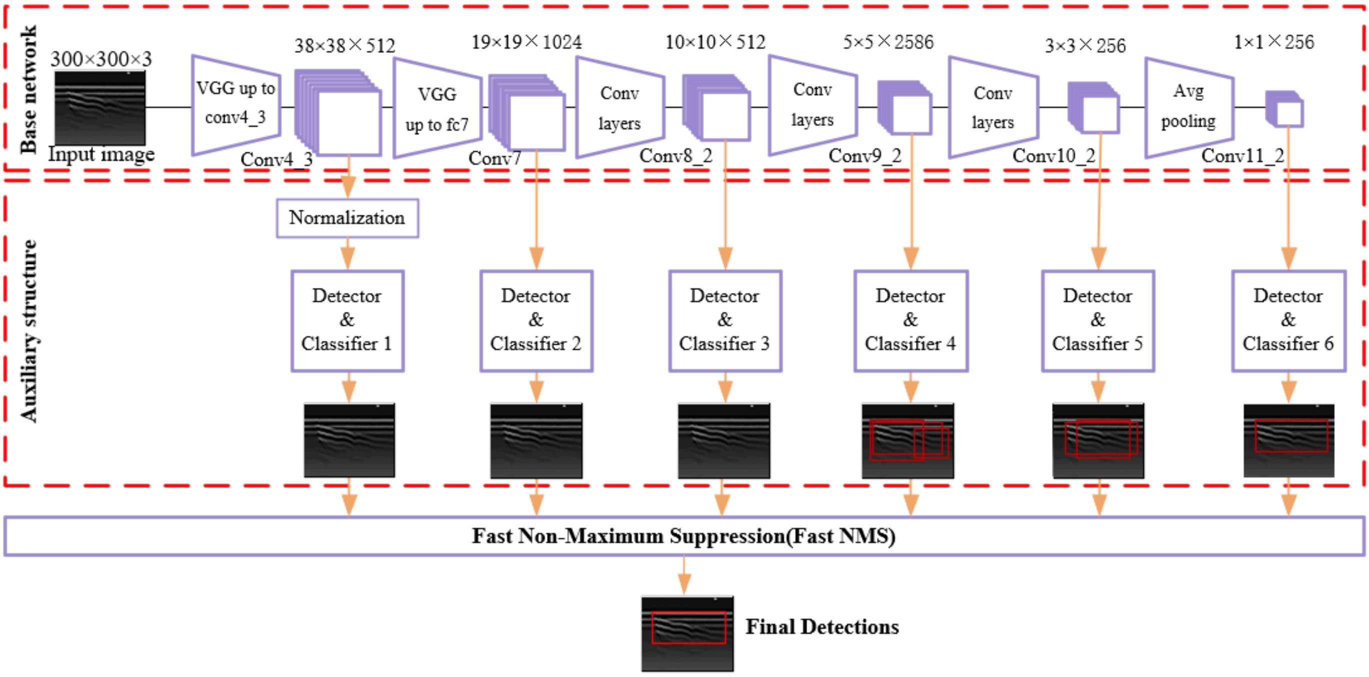

Figure 3. SSD model framework for quality defect recognition in GPR images.

2.4. YOLOv4

The YOLO series is a popular one-stage object detection algorithm that has evolved into the stable YOLOv4 version [30]. It segments the input image into distinct scale grids where each grid is accountable for its corresponding area. If the center of a detected object is located within a specific grid, the corresponding grid detects the object. Figure 4 illustrates the three-part network structure of YOLOv4: the backbone network, responsible for feature extraction; the Neck, for multi-scale feature fusion; and the Prediction, for object detection and output.

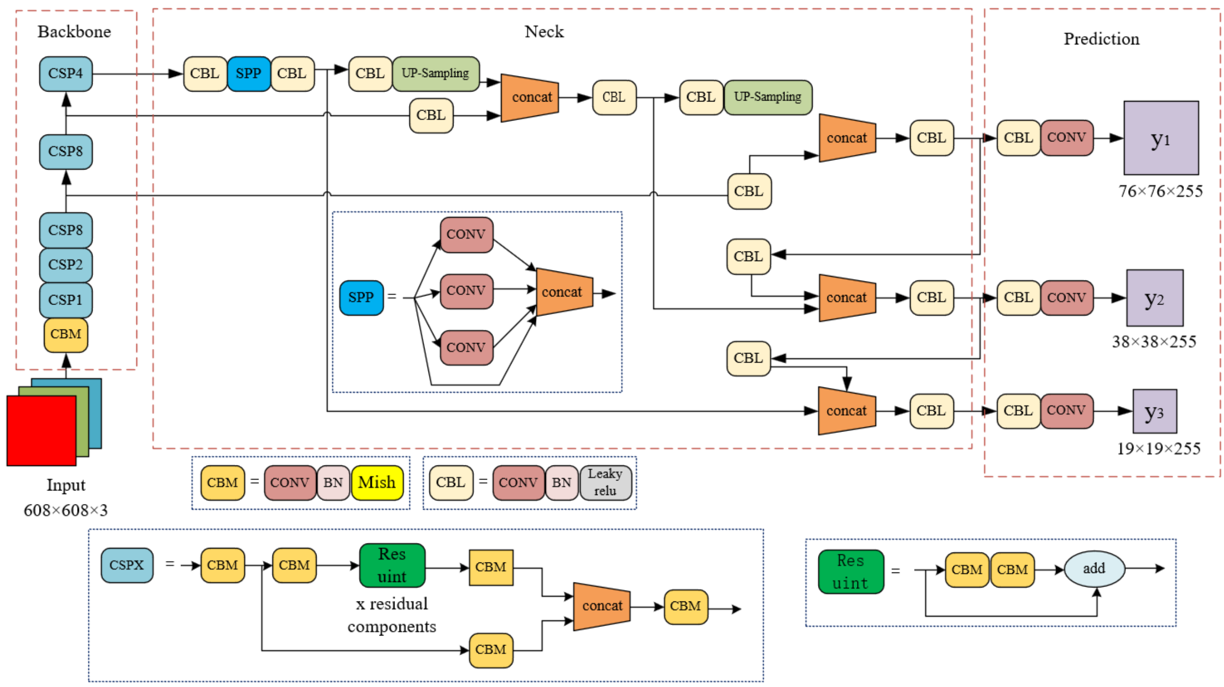

Figure 4. YOLOv4 algorithm model structure diagram.

The YOLOv4 optimization, when compared to YOLOv3, can be divided into four main areas: (1) the backbone network, which replaced the original Leaky ReLU activation function post-initial convolutional layer with Mish, by drawing from CSPNet; (2) the Neck part, which expanded the receptive field of the network and separated salient context semantic information by adding a Spatial Pyramid Pooling (SPP) module after the backbone network, using different scale pooling layers to process the end feature layer; (3) the integration of multi-scale feature maps, which was fully realized by using the "bottom-up" feature pyramid structure in PANet; and (4) the loss function, which integrated the anchor box width and height and the coordinate information of the center point to use CIOU instead of the mean squared error MSE used in the bounding box regression of YOLOv3.

During the final Prediction phase of YOLOv4, the three feature layers that have been processed by the feature pyramid part of PANet will be predicted. Similar to YOLOv3, each prior box in each feature layer is discriminated, which involves determining whether it contains the detected target and its category. The final detection outcomes are then produced by non-maximum suppression and bounding box position adjustment.

2.5. Non-Maximum Suppression

The SSD and YOLOv4 algorithms in object detection produce multiple candidate boxes, some of which may be invalid. To remove invalid boxes, the non-maximum suppression (NMS) algorithm is utilized before the ultimate output of the prediction. The NMS algorithm operates by sorting the predicted candidate boxes and selecting the box with the highest confidence, after which a threshold is established. The Intersection over Union (IoU) or Distance IoU ($DIoU$) value (for SSD or YOLOv4, respectively) is then determined between this box and the rest of the boxes, as denoted in Equations (1) and (2). Finally, the $IoU/DIoU$ value is compared to the threshold. If the value exceeds the threshold, it suggests that both boxes predict the same object and the box with lower confidence should be removed. Otherwise, the box with higher confidence will be chosen for the succeeding computation. Through this iterative procedure, NMS can be accomplished. The process of NMS is illustrated in Figure 5.

$$IOU = \frac{A \cap B}{A \cup B} \tag{1}$$

$$DIOU = IOU - \frac{\rho^2(b, b^{zs})}{c^2} \tag{2}$$

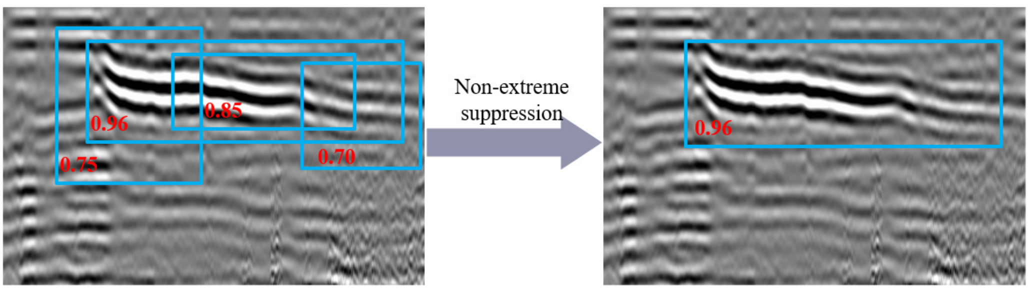

Figure 5. Schematic diagram of non-maximum suppression.

The formula involves candidate frames represented by A and B, where b denotes the center coordinates of the predicted frame and b^{zs} denotes the real frame center coordinates. Euclidean distance is denoted by ρ and c indicates the length of the diagonal of the circumscribed rectangle of the two bounding boxes for the target.

2.6. Transfer Learning

To avoid the overfitting of the CNN model, a sufficient number of training data is required. Nonetheless, generating effective GPR profiles is more arduous, owing to the additional time and labor required compared to natural photographs. Therefore, to tackle this issue, transfer learning was employed in this study. Transfer learning is a novel supervised learning strategy which involves utilizing the pre-trained network model parameters from a huge dataset. These parameters can then be embedded into other task models such as feature extractors. As illustrated in Figure 6, the model was trained in the source domain, and the knowledge acquired from the convolutional neural network and source domain was transferred to the target domain. Thereafter, a new classification layer was created that joined the transferred network model to a new convolutional neural network. This composite network was then employed to train the image data of the target domain. To guarantee exceptional detection capabilities of the pre-trained CNN model, we performed pre-training using the PASCAL VOC2007 dataset. This dataset covers 20 categories with 9963 images. After pre-training, the weight parameters of the base structure of the model were extracted to train and fine-tune the task model using the GPR dataset. The transfer learning method is an efficient approach in which the demand for computer resources is minimized. This leads to faster training convergence and saves time during training.

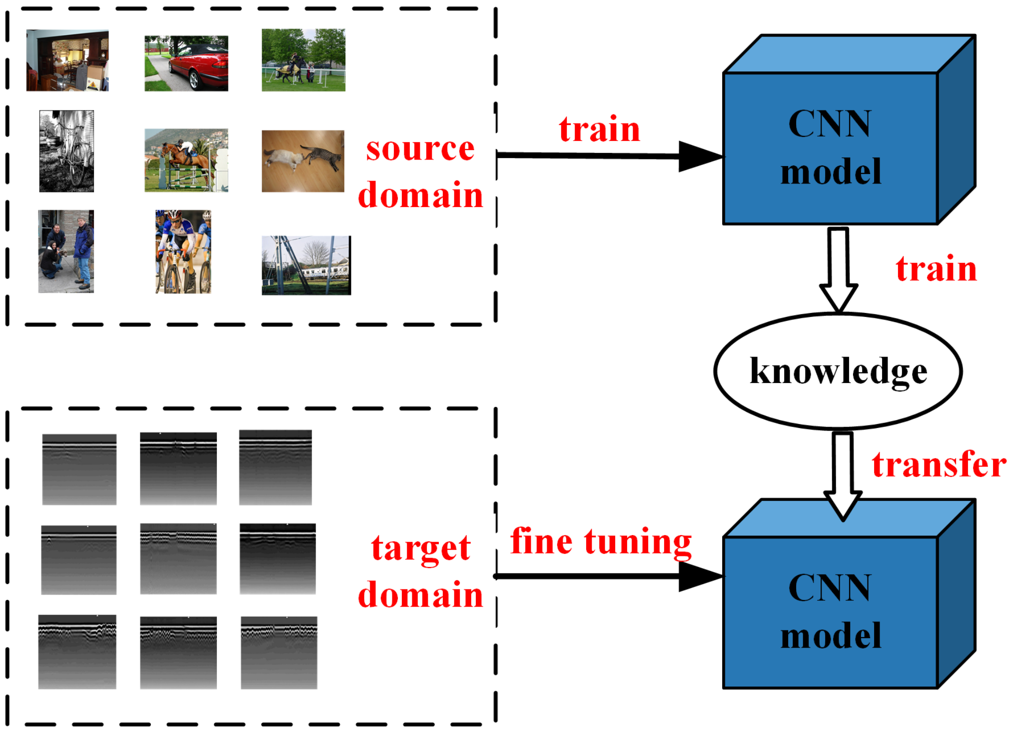

Figure 6. Migration learning process.

3. Real Dataset for Deep Learning

3.1. Collection of Real Radar Data on Site

The preeminent factors essential for training a detection model are the quantity and quality of datasets. However, presently, there are limited studies focusing on geological radar images for tunnel detection, and such datasets are not available for public download similar to datasets such as VOC and ImageNet. Undoubtedly, some scholars have resorted to the FDTD method to simulate and evaluate radar data of tunnel defects, which has enabled the acquisition of new data. Nonetheless, radar data obtained through numerical simulation can never be as authentic compared to the measured data, thus diverging from the features of measured data. Consequently, to obtain high-quality datasets, we collected a huge number of ground-penetrating radar images during lining quality inspection work at several tunnel engineering sites, as illustrated in Figure 7. These GPR images consist of many samples containing locally deficient steel bars and inner-cavity defects in tunnel lining. During data collection, no filters or gain processing were applied.

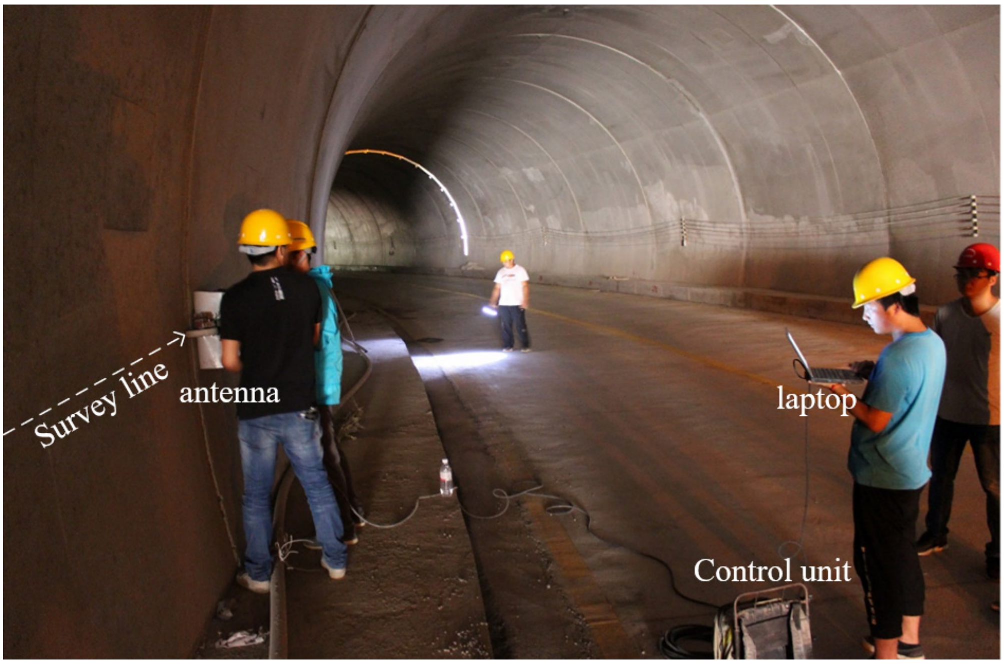

Figure 7. GPR data acquisition map of tunnel lining quality inspection.

3.2. Lining Detection Model Test

The proper analysis of radar data hinges upon the proficiency of the detection personnel. To prevent misjudgment or omissions due to insufficient expertise, a detection model for tunnel linings was developed, containing typical defects. Radial image features for typical quality faults were established by amalgamating the collected lining radar data images and the designed lining model. This laid a foundation for the establishment of data samples.

3.2.1. Design and Establishment of Lining Model

Lining defects in highway tunnels mainly occur in the surrounding rocks of Grade III, IV, and V [31]. To obtain reliable data for comparison regarding typical lining defects and to simulate practical construction situations, this study created standard lining models (corresponding to the surrounding rocks of Grade III, IV, and V) and typical defect lining models in a 1:1 proportion.

The standard lining model consists of one lining wall without defects in each of the surrounding rocks of Grade III, IV, and V. The model is 8 m in length and 1.5 m in height, featuring a 5 cm-thick concrete protective layer on both the rock-stabilized and internal sides of the vertical steel bars. Each steel arch has a length of 1.7 m, and the vertical main steel bars are uniformly 1.65 m apart.

The typical defect lining model includes three 20 m-long and 1.5 m-high lining walls, each with the same 5 cm-thick concrete protective layer on both the rock-stabilized and internal sides of the vertical steel bars. Each steel arch has a length of 1.7 m, and the vertical main steel bars are uniformly 1.65 m apart. The walls of the lining contain defects such as empty spaces in the secondary lining, cavity defects, missing steel bars, and insufficient thickness in the secondary lining.

Arranged as shown in Figure 8, the lining detection models simulate the specific structural dimensions of the tunnel lining side walls during construction. Walls 1 to 3 are standard lining walls without defects, while Walls 4 to 6 are lining walls with local defects, as illustrated in Figure 9.

Figure 8. Overall layout of the lining model.

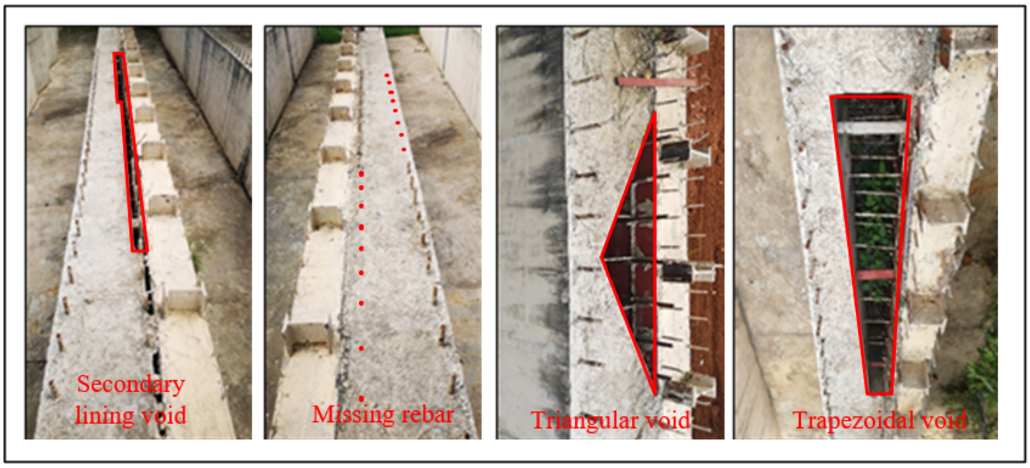

Figure 9. Visual view of typical defects of lining model.

3.2.2. Acquisition of Ground Radar Signals

The field research site uses the Swedish MALA ground penetrating radar RAMAC/GPR X3M host, with a shielded 500 MHz center frequency antenna for data collection. The equipment information and collection parameters are shown in Table 1. Figure 10 depicts the on-site detection process.

Table 1. Equipment Information and Acquisition Parameters.

GPR System	Antenna Center Frequency (MHz)	Sampling Frequency (MHz)	Samples per Scan	Time Window (ns)	Sampling Interval (cm)	Trigger Mode
MALA (X3M)	500	7500	512	50	2	Distance-based

The data collection, processing, and analysis use the instrument's proprietary acquisition and analysis software Ground Vision (latest v2.1) and REFLEXW (latest v10). The data files are preprocessed, gain adjusted, filtered, and imaged to obtain the final radargrams for each survey line.

The main preprocessing includes: (1) Editing acquisition information; (2) Correcting milepost numbers; (3) Adjusting thickness scales.

The image filtering process has six steps: (1) Static correction; (2) DC drift removal; (3) Overflow removal; (4) Horizontal signal removal; (5) Bandpass filtering; (6) Sliding average.

Figure 10. On-site inspection diagram of lining model.

3.2.3. Radar Image Features of Typical Quality Defects

This article focuses on two common defects: lining void and steel bar loss. We describe the typical radar image characteristics of each separately.

- Lining void

A lining void is an empty space that lies beneath the tunnel lining, resulting from a gap between the lining and surrounding rock. As depicted in Figure 11, a massive discrepancy in the dielectric constants of air and concrete creates a notable gap between the lining and rock, observable as intensified reflection signals at the lining interface within geological radar images. In the event that the cavity size is significant, diffraction signals occur beneath the interface signal. In tandem with a radar waveform analysis, we can scrutinize transformations in a hyperbolic waveform.

- Steel bar loss

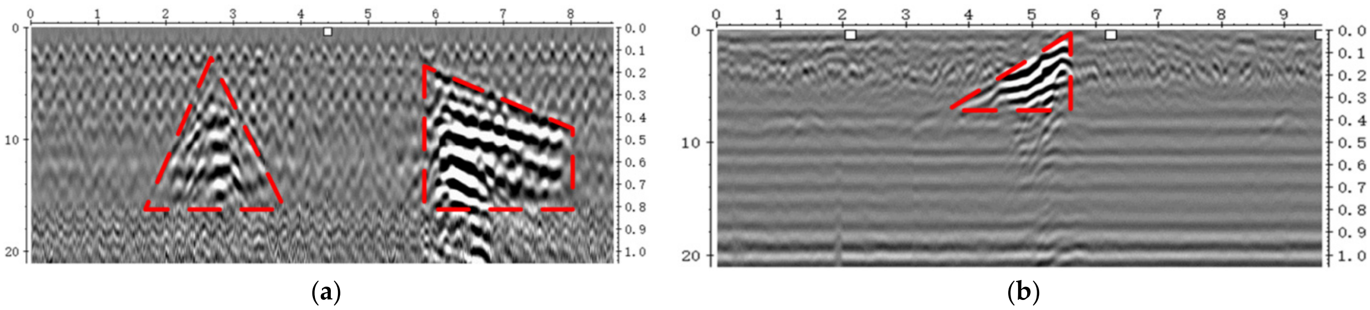

Figure 11. Geological radar image of lining void. (**a**) Reinforced concrete model wall; (**b**) Plain concrete model wall.

Steel bar loss is a common issue during tunnel construction, resulting in a reduced carrying capacity of the tunnel compared to the design requirements. According to Figure 12, steel bars cause continuous, point-like reflections due to their high relative dielectric constant, which is greater than that of the lining concrete. A single steel bar's waveform is an upwardly convex arc, with its crest representing the top of the steel bar. The arrangement of multiple steel bars side by side leads to non-standard arc shapes of steel bars on the radar image due to the effects of their size, spacing, electromagnetic wave diffraction, and radar resolution on adjacent steel bars. To determine if the design requirements are met, the number of steel bars within a specific distance is counted during the detection process, allowing for the calculation of steel bar quantity and spacing.

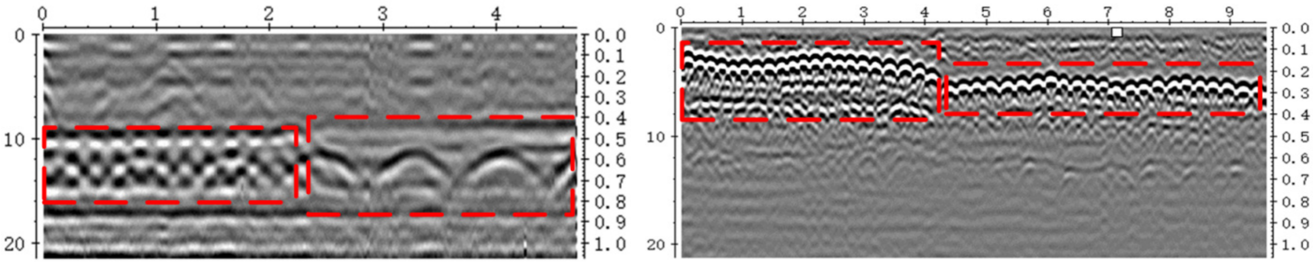

(**a**) (**b**)

Figure 12. Geological radar image of missing main reinforcement of lining. (**a**) Single layer with reinforcement and no reinforcement; (**b**) Double-layer and single-layer bars.

3.3. Processing of Data

Pulse radar records medium reflection information, but radar waves attenuate as the detection depth increases, resulting in less clear information. Image gain processing is necessary to enhance recorded information during radar data processing. Following gain processing, noise clutter is more noticeable and can be eliminated by filtering methods. In addition to conventional gain processing, the radar image dataset is preprocessed for mean removal, normalization, and size adjustment before inputting it into the SSD and Yolov4 models with respective image sizes of 300 × 300 and 416 × 416 pixels. To enhance the performance and robustness of the neural network, a data augmentation strategy is adopted to create a GPR dataset. As the number of GPR images directly affects performance, mirror flipping and cropping are applied to increase image size for training. Mirror flipping and cropping enhance the image's spatial complexity without changing the primary defect characteristics. A dataset size of 4246 is achieved by image transformation, fulfilling the training sample requirement while enhancing the model's generalization. Figure 13 illustrates the processing of the radar image data.

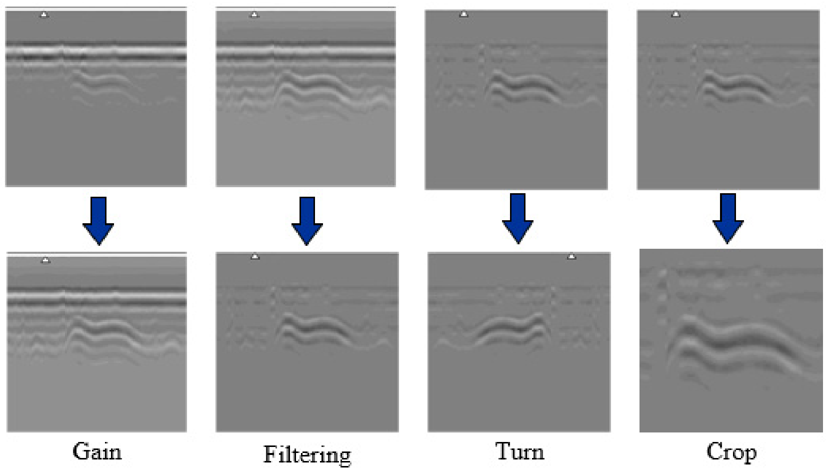

Figure 13. Processing of radar image data.

Dataset annotation entails annotating tunnel defect category information and defect locations in the data image. The LabelImg software is a Python-written graphical image annotation tool we used for dataset annotation. After opening the radar image in the LabelImg software (latest v1.8.6), the corresponding position is selected using a labeled box in the software and defect category specified upon identifying the tunnel defect feature in the image. Saving defect category and location information as VOC format (.xml) files follows the aforementioned operation. Every image in the dataset requires annotation to create a unique xml file for that image. Upon being placed into two separate folders, the images and xml files are collectively inputted into the network model for training. This method enables the model to interpret the corresponding image's defect features through the xml file.

4. Results and Discussions

4.1. Analysis of Prediction Effect of Tunnel Defect Identification Model

To confirm the actual predictive capability of the defect recognition model after training, we utilized non-preprocessed and labeled non-training samples to perform experimental verification. Figures 14 and 15 display the identification prediction effects outputted by the model.

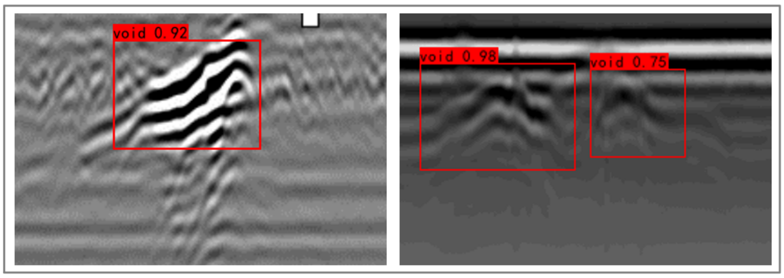

(**a**)

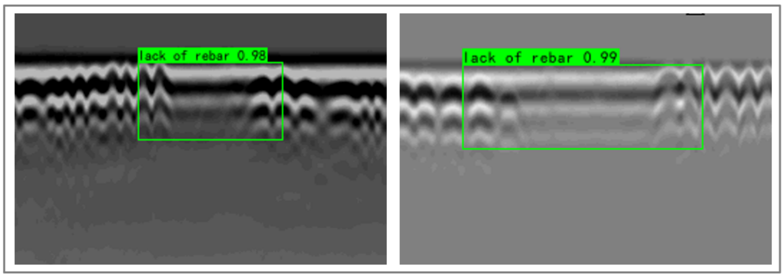

(**b**)

Figure 14. Prediction effect of defect recognition model based on SSD algorithm. (**a**) Detect voids; (**b**) Rebar defects.

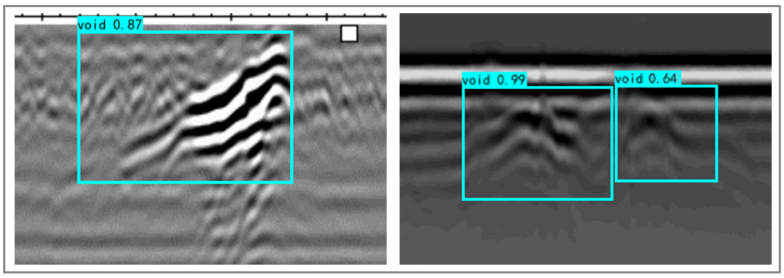

(**a**)

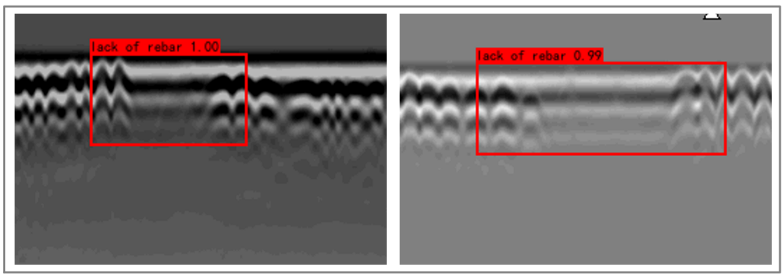

(**b**)

Figure 15. Prediction effect of defect recognition model based on YOLOv4 algorithm. (**a**) Detect voids; (**b**) Rebar defects.

The prediction diagram of the tunnel defect recognition model indicates that both the SSD and YOLOv4 algorithms are effective in identifying defects in both the cavity and reinforcing bar radar images with high accuracy in defect categorization and localization.

The SSD algorithm presented prediction probabilities of 0.90, 0.97, and 0.67 for the cavity defect. Likewise, the predictions of the YOLOv4 algorithm for the cavity defect were 0.75, 0.99, and 0.64, respectively. The SSD algorithm shows slightly better performance than the YOLOv4 algorithm regarding the radar images of the same defect, but the difference is marginal. The output probabilities of both algorithms for the reinforcing bar defect are almost equal to 1, with the YOLOv4 algorithm producing a prediction probability of 1 for some defects. In conclusion, object detection based on deep learning techniques demonstrates strong potential for interpreting and recognizing radar images.

4.2. Accuracy Analysis of Tunnel Defect Recognition Model

The prediction of the tunnel defect recognition model provides clear information regarding the location and category of defects. In addition, the *AP* value, jointly determined by precision and recall, provides a precise measure of the model's average accuracy in detecting defects in each category. This paper evaluates the recognition accuracy of the model using the P-R curve and *AP* values. The evaluation metric formulas are as follows:

$$Precision = \frac{TP}{TP + FP} \tag{3}$$

$$Recall = \frac{TP}{TP + FN} \tag{4}$$

$$AP = \int_0^1 P(r)dr \tag{5}$$

where: *AP* refers to average precision, *TP* is the total number of correct recognitions, *FP* is the total number of incorrect recognitions, and *FN* is the total number of missed recognitions.

The Precision-Recall (P-R) curves for the tunnel defect identification model based on the test results of the SSD algorithm and YOLOv4 algorithm are shown in Figure 16, and the average precision (*AP*) values are presented in Figure 17.

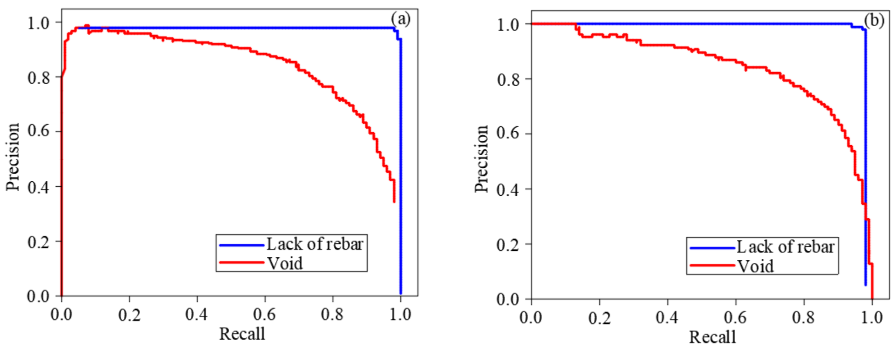

Figure 16. P-R curves of test results. (**a**) The precision-recall curve of YOLOv4 for object detection; (**b**) The precision-recall curve of SSD for object detection.

This paper adopts the conventional approach of defining identification accuracy as: correct classification and *IoU* > 0.5. The P-R curve depicts the relationship between precision and recall, which are a pair of conflicting metrics—generally when precision is high, recall tends to be low. For recognition algorithms, we desire both high precision and recall, and therefore the closer the P-R curve is to the top right corner, the better. As shown in Figure 16, the P–R curves for both categories are close to the top right corner. In identifying rebar absence, both methods achieve relatively good performance—maintaining high precision while also achieving good recall. However, the recognition performance for voids is poorer.

Figure 16 demonstrates that the SSD and YOLOv4 algorithms have high recognition accuracy when identifying lining quality defects. While the recognition accuracy of cavity defects for the SSD algorithm is 86.58%, that of the YOLOv4 algorithm is slightly lower at 86.05%; both algorithms still show similar recognition effects. On the other hand, both algorithms exhibit higher recognition accuracy when it comes to identifying reinforcing bar defects. The SSD algorithm can recognize reinforcing bar defects with an accuracy rate of 97.7%, while the YOLOv4 algorithm can recognize it with 98.18%, indicating that it has a slightly higher recognition rate than the former. The recognition effect of the two algorithms varies in identifying cavity and reinforcing bar defects. The complex shape and feature information of cavity defects increase the difficulty of feature extraction and recognition during model training, which is responsible for the variation in recognition effects. Both algorithms exhibit extremely accurate rates, confirming the feasibility and usefulness of the defect recognition model in detecting tunnel defects.

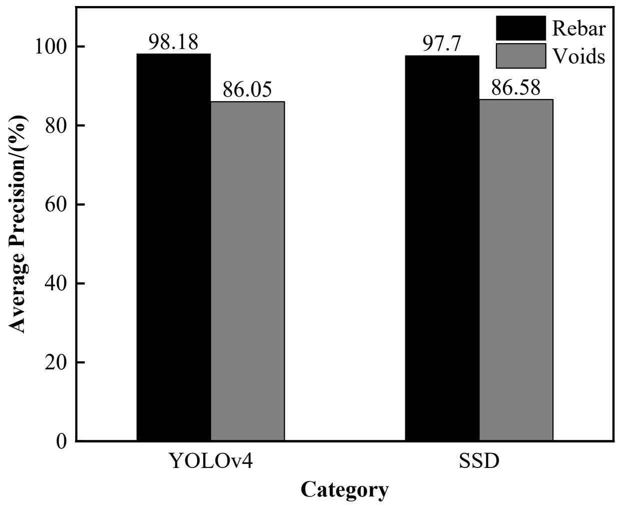

Figure 17. *AP* value of tunnel defect identification model.

4.3. Comprehensive Performance Analysis of Tunnel Defect Recognition Model

In addition to the primary mAP value, evaluating an algorithm also requires consideration of its training complexity and the required model size for specific use cases. The mAP value indicates the defect recognition model's overall recognition accuracy and generalization, while training time and model size affect the time and space costs of recognition detection. Table 2 clearly indicates that both tunnel defect recognition model algorithms achieve high accuracy levels, exceeding 92%, and demonstrate strong generalization. Even though the YOLOv4 algorithm has a slightly inferior 0.02% accuracy rate compared to the SSD algorithm and is larger in size, it takes only one-third of the SSD algorithm's training time, and its detection frame rate is twice as fast. Despite training time and detection frame rate being notably impacted by computer performance, the YOLOv4 algorithm demonstrates significantly lower time costs in this paper's experimental environment. Consequently, with the current rapid hardware advancements, the YOLOv4 algorithm is more suitable for quick detection operations.

Table 2. Comparison of comprehensive performance between YOLOv4 and SSD algorithm recognition models.

Model	mAP (%)	Size (MB)	Time (h)	Rate (FPS)
SSD	92.14	93	23.5	36.84
YOLOv4	92.12	246	8	70.52

5. Conclusions

The study discusses the high cost, time-consuming, and low-efficiency issues in conventional tunnel detection methods. The study proposes a deep learning algorithm framework for predicting internal defects in tunnel linings using actual radar data and transfer learning. The framework aims to address the issue of detecting defects in tunnel linings through ground-penetrating radar images.

Standard radar image features of typical defects were determined through field and model experiments. Moreover, a data sample set with 6236 detection targets was obtained after analyzing 4246 images representing typical quality defects in tunnel linings.

The transfer of pre-trained weights from the SSD and YOLOv4 algorithm models to the tunnel defect recognition model enabled detecting and recognizing tunnel quality defects. The results indicated that both types of deep learning algorithms significantly predicted tunnel cavity defects, with an accuracy rate of over 86%. Additionally, the accuracy rate for reinforcing bar defects was as high as 98.18%. These findings indicate that deep learning models have practical potential for tunnel quality defect detection.

Both the SSD and YOLOv4 algorithm models exhibit high average precision values (mAP) and retain strong detection capabilities and generalizations while handling complex geological radar images. They have varying characteristics such as model size and training time. The YOLOv4 algorithm, in general, presents better applicability and potential for application.

Due to the limited number and types of samples, the deep learning-based tunnel lining defect prediction method proposed in this study still needs further validation for identifying other types of lining defects. Future research will continue to enrich the sample library, expand the categories of defects, and optimize the network structure to improve its generalization ability. In addition, different engineering environments may lead to differences in image features, and more engineering verification is needed to improve the robustness of the model.

Author Contributions: Methodology, P.L.; Project administration, Z.D.; Resources, Z.R.; Software, W.Z.; Supervision, X.Y.; Writing—original draft, P.L. All authors have read and agreed to the published version of the manuscript.

Funding: This research was funded by the National Natural Science Foundation of China, grant number 52168057; Technology Project of Yunnan Provincial Department of Transportation, grant number 2022-23-1; Yunnan Science and Technology Department Project, grant number 202303AA080003.

Institutional Review Board Statement: Not applicable.

Informed Consent Statement: Not applicable.

Data Availability Statement: For privacy reasons, the data cannot be made fully public. Readers can contact the corresponding author for details.

Conflicts of Interest: The authors declare no conflict of interest.

Abbreviations

GPR	Ground-penetrating radar
SSD	Single Shot MultiBox Detector
YOLO	You Only Look Once
AP	Average Precision
mAP	Mean Average Precision
FDTD	Finite-difference Time-domain

References

1. Hong, K.; Feng, H. Development Trends and Views of Highway Tunnels in China over the Past Decade. *China J. Highw. Transp.* **2020**, *33*, 62–76.
2. Lu, F.; Wang, Y.; Fu, J.; Yang, Y.; Qiu, W.; Jing, Y.; Jiang, M.; Li, H. Safety Evaluation of Plain Concrete Lining Considering Deterioration and Aerodynamic Effects. *Sustainability* **2023**, *15*, 7170. [CrossRef]
3. Popovics, S.; Rose, J.L.; Popovics, J.S. The behaviour of ultrasonic pulses in concrete. *Cem. Concr. Res.* **1990**, *20*, 259–270. [CrossRef]
4. Le Sant, Y.; Marchand, M.; Millan, P.; Fontaine, J. An overview of infrared thermography techniques used in large wind tunnels. *Aerosp. Sci. Technol.* **2002**, *6*, 355–366. [CrossRef]
5. Li, S.; Zhou, Z.; Ye, Z.; Li, L.; Zhang, Q.; Xu, Z. Comprehensive geophysical prediction and treatment measures of karst caves in deep buried tunnel. *J. Appl. Geophys.* **2015**, *116*, 247–257. [CrossRef]
6. Liu, M.; Liu, Z.; Zhou, D.; Lan, R.; Wu, H. Recognition method of typical anomalies during karst tunnel construction using GPR attributes and Gaussian processes. *Arab. J. Geosci.* **2020**, *13*, 1–13. [CrossRef]

7. Liu, Z.; Wu, Y.; Liu, B.; Liu, M.; Lan, R.; Sun, H. Research on the interference elimination method of GPR signal for tunnel geological prediction. *Chin. J. Eng.* **2020**, *42*, 390–398.
8. Liu, B.; Zhang, F.; Li, S.; Li, Y.; Xu, S.; Nie, L.; Zhang, C.; Zhang, Q. Forward modelling and imaging of ground-penetrating radar in tunnel ahead geological prospecting. *Geophys. Prospect.* **2018**, *66*, 784–797. [CrossRef]
9. Luo, G.; Cao, Y.; Xu, H.; Yang, G.; Wang, S.; Huang, Y.; Bai, Z. Research on typical soil physical properties in a mining area: Feasibility of three-dimensional ground penetrating radar detection. *Environ. Earth Sci.* **2021**, *80*, 1–11. [CrossRef]
10. Zheng, A.; Zhao, H.; Tan, B.; Huang, F.; He, Z. Radar Image Recognition of Tunnel Lining Cavity Fillings Based on SVM. *Mod. Tunn. Technol.* **2022**, *59*, 45–52.
11. Liu, H.; Deng, Z.; Han, F.; Xia, Y.; Liu, Q.H.; Sato, M. Time-frequency analysis of air-coupled GPR data for identification of delamination between pavement layers. *Constr. Build. Mater.* **2017**, *154*, 1207–1215. [CrossRef]
12. Benedetto, A.; Tosti, F.; Ciampoli, L.B.; D'amico, F. An overview of ground-penetrating radar signal processing techniques for road inspections. *Signal Process.* **2017**, *132*, 201–209. [CrossRef]
13. Li, W.; Cui, X.; Guo, L.; Chen, J.; Chen, X.; Cao, X. Tree root automatic recognition in ground penetrating radar profiles based on randomized Hough transform. *Remote Sens.* **2016**, *8*, 430. [CrossRef]
14. Zhixin, Z.; Shuhao, J. Design of incomplete 3D information image recognition system based on SIFT algorithm and wireless network. *EURASIP J. Wirel. Commun. Netw.* **2020**, *2020*, 1–20. [CrossRef]
15. Xie, X.; Li, P.; Qin, H.; Liu, L.; Nobes, D.C. GPR identification of voids inside concrete based on the support vector machine algorithm. *J. Geophys. Eng.* **2013**, *10*, 034002. [CrossRef]
16. Long, J.; Shelhamer, E.; Darrell, T. Fully Convolutional Networks for Semantic Segmentation. In Proceedings of the IEEE Conference on Computer Vision and Pattern Recognition, Boston, MA, USA, 7–12 June 2015; Volume 2015, pp. 3431–3440.
17. Ronneberger, O.; Fischer, P.; Brox, T. U-Net: Convolutional Networks for Biomedical Image Segmentation. In Proceedings of the Medical Image Computing and Computer-Assisted Intervention–MICCAI 2015: 18th International Conference, Munich, Germany, 5–9 October 2015; Springer: Berlin/Heidelberg, Germany, 2015; pp. 234–241.
18. Badrinarayanan, V.; Kendall, A.; Cipolla, R. Segnet: A deep convolutional encoder-decoder architecture for image segmentation. *IEEE Trans. Pattern Anal. Mach. Intell.* **2017**, *39*, 2481–2495. [CrossRef]
19. Xu, Y.; Mo, T.; Feng, Q.; Zhong, P.; Lai, M.; Eric, I.; Chang, C. Deep Learning of Feature Representation with Multiple Instance Learning for Medical Image Analysis. In Proceedings of the 2014 IEEE International Conference on Acoustics, Speech and Signal Processing (ICASSP), Florence, Italy, 4–9 May 2014; pp. 1626–1630.
20. Kayalibay, B.; Jensen, G.; van der Smagt, P. CNN-based segmentation of medical imaging data. *arXiv* **2017**, arXiv:1701.03056.
21. Li, S.; Liu, B.; Ren, Y.; Chen, Y.; Yang, S.; Wang, Y.; Jiang, P. Deep-learning inversion of seismic data. *arXiv* **2019**, arXiv:1901.07733. [CrossRef]
22. Liu, B.; Guo, Q.; Li, S.; Liu, B.; Ren, Y.; Pang, Y.; Guo, X.; Liu, L.; Jiang, P. Deep learning inversion of electrical resistivity data. *IEEE Trans. Geosci. Remote Sens.* **2020**, *58*, 5715–5728. [CrossRef]
23. Huang, H.-W.; Li, Q.-T.; Zhang, D.-M. Deep learning based image recognition for crack and leakage defects of metro shield tunnel. *Tunn. Undergr. Space Technol.* **2018**, *77*, 166–176. [CrossRef]
24. Ren, Y.; Huang, J.; Hong, Z.; Lu, W.; Yin, J.; Zou, L.; Shen, X. Image-based concrete crack detection in tunnels using deep fully convolutional networks. *Constr. Build. Mater.* **2020**, *234*, 117367. [CrossRef]
25. Yang, S.; Wang, Z.; Wang, J.; Cohn, A.G.; Zhang, J.; Jiang, P.; Nie, L.; Sui, Q. Defect segmentation: Mapping tunnel lining internal defects with ground penetrating radar data using a convolutional neural network. *Constr. Build. Mater.* **2022**, *319*, 125658.
26. Qin, H.; Zhang, D.; Tang, Y.; Wang, Y. Automatic recognition of tunnel lining elements from GPR images using deep convolutional networks with data augmentation. *Autom. Constr.* **2021**, *130*, 103830. [CrossRef]
27. Ye, Z.; Ye, Y. Comparison of Detection Effect of Cavities Behind Shield Tunnel Segment Using Transient Electromagnetic Radar and Ground Penetration Radar. *Geotech. Geol. Eng.* **2019**, *37*, 4391–4403. [CrossRef]
28. Liu, W.; Anguelov, D.; Erhan, D.; Szegedy, C.; Reed, S.; Fu, C.-Y.; Berg, A.C. Ssd: Single Shot Multibox Detector. In Proceedings of the Computer Vision–ECCV 2016: 14th European Conference, Amsterdam, The Netherlands, 11–14 October 2016; Springer: Berlin/Heidelberg, Germany, 2016; pp. 21–37.
29. Simonyan, K.; Zisserman, A. Very deep convolutional networks for large-scale image recognition. *arXiv* **2014**, arXiv:1409.1556.
30. Bochkovskiy, A.; Wang, C.-Y.; Liao, H.-Y.M. Yolov4: Optimal speed and accuracy of object detection. *arXiv* **2020**, arXiv:2004.10934.
31. Zhong, B. *Study on the Damage Characteristics and Service Status Evaluation Methods of Highway Tunnel Lining in Yunnan Mountain Area*; University of Science and Technology: Kunming, China, 2018.